



# Nature of TiO<sub>2</sub>–oligonucleotides interactions by atomistic molecular dynamics simulations

Federico A. Soria<sup>a,b</sup>, Paulo Siani<sup>a</sup>, Cristiana Di Valentin<sup>a,c,\*</sup>

<sup>a</sup> Dipartimento di Scienza dei Materiali, Università di Milano Bicocca, via R. Cozzi 55 20125 Milano Italy

<sup>b</sup> Departamento de Química Teórica y Computacional. Instituto de Investigaciones en Físico Química de Córdoba (INFIQC-CONICET). Facultad de Ciencias Químicas, Universidad Nacional de Córdoba, X5000HUA Córdoba, Argentina

<sup>c</sup> BioNanoMedicine Center NANOMIB, University of Milano-Bicocca, Italy

## ARTICLE INFO

### Keywords:

DNA  
Anatase  
Molecular dynamics  
Oligonucleotides  
Adsorption mechanism  
Nucleobasis

## ABSTRACT

We used molecular dynamics simulations to investigate the adsorption behavior of single-stranded deoxy-ribonucleic acid (ssDNA) segments on the anatase (101) surface. Four different ssDNA oligonucleotides, each consisting of six/twelve adenine (A6 and A12), six guanine (G6), six cytosine (C6) or six/twelve thymine (T6 and T12) nucleobases, were considered. We observed that the initial interaction between the ssDNA and the surface occurs primarily through hydrogen bonding between the nucleobases and the surface, followed by strong chemical bonding between the terminal phosphate group and the anatase surface. The interactions between the nucleobases and the surface varied between the different ssDNA segments. Adenine showed the highest affinity for the surface, whereas thymine showed the lowest affinity. In addition, the purine bases interact more strongly when the surface is negatively charged (as it would be at physiological pH) than in neutral surface (slightly acidic conditions), in agreement with experimental data from fluorescence experiments and ATR-FTIR spectroscopy. Moreover, our study provides mechanistic insights into the dynamic behavior of ssDNA on the anatase surface and comparative analyses on how different conditions (pH, fragment length, composition, etc.) affect DNA/TiO<sub>2</sub> interactions. Therefore, we expect that experimental scientists will benefit from our work in the design of optimal nanoconjugates for their specific final goals and applications.

## 1. Introduction

DNA-based nanoconjugates combine the inherent programming abilities of DNA with the intrinsic physical properties of inorganic nanoparticles. This unique combination allows for the regulation of optical, electrical, and magnetic responses, as well as the ability to achieve high local biomolecular concentrations. As a result, these nanostructures have the potential to offer novel detection approaches and functional applications [1,2].

Titanium dioxide (TiO<sub>2</sub>) nanoparticles (NPs) are highly effective in applications such as photocatalysis [3,4], photoelectrochemistry [5], photovoltaics [6,7], and photochromic devices [8], due to their ability to convert light photons into chemical processes. Recently, their potential in nanomedicine has gained interest, particularly in photodynamic therapy for tumors and photoinduced drug release [9]. DNA-TiO<sub>2</sub> nanoconjugates, in particular, have shown promise for applications in biomedicine [9], water treatment [10], genetic and infectious disease

diagnostic devices [11,12] and miniaturized biosensor arrays [13].

The molecular functionalization of TiO<sub>2</sub> surfaces can be tailored for specific functions, such as drug transport [14], targeting therapy [15] or effective modulation of protein corona [16]. Conjugation with single-stranded or double-stranded DNA has been achieved through both direct [17–19] (DNA interacting directly with the TiO<sub>2</sub> surface) and indirect attachment (DNA fragments are covalently attached to a linker, which is immobilized to the surface of TiO<sub>2</sub> nanoparticles due to electrostatic interactions) [20]. In the first case, experimental findings indicate that the degree of DNA adsorption is pH-dependent: under neutral conditions, binding primarily occurs through the backbone phosphate, with the nucleobases engaging the surface through electrostatic interactions, resulting in a parallel adsorption configuration. Conversely, at pH 2, the DNA's adsorption capacity increases drastically due to the protonation of nucleobases, which prevents their interaction with the surface. This results in an upright adsorption configuration and denser packing of DNA chains [17,18]. In a recent experimental study

\* Corresponding author at: Dipartimento di Scienza dei Materiali, Università di Milano Bicocca, via R. Cozzi 55 20125 Milano Italy.

E-mail address: [cristiana.divalentin@unimib.it](mailto:cristiana.divalentin@unimib.it) (C.D. Valentin).

<https://doi.org/10.1016/j.surfin.2024.104889>

Received 8 April 2024; Received in revised form 26 July 2024; Accepted 30 July 2024

Available online 2 August 2024

2468-0230/© 2024 The Authors. Published by Elsevier B.V. This is an open access article under the CC BY license (<http://creativecommons.org/licenses/by/4.0/>).

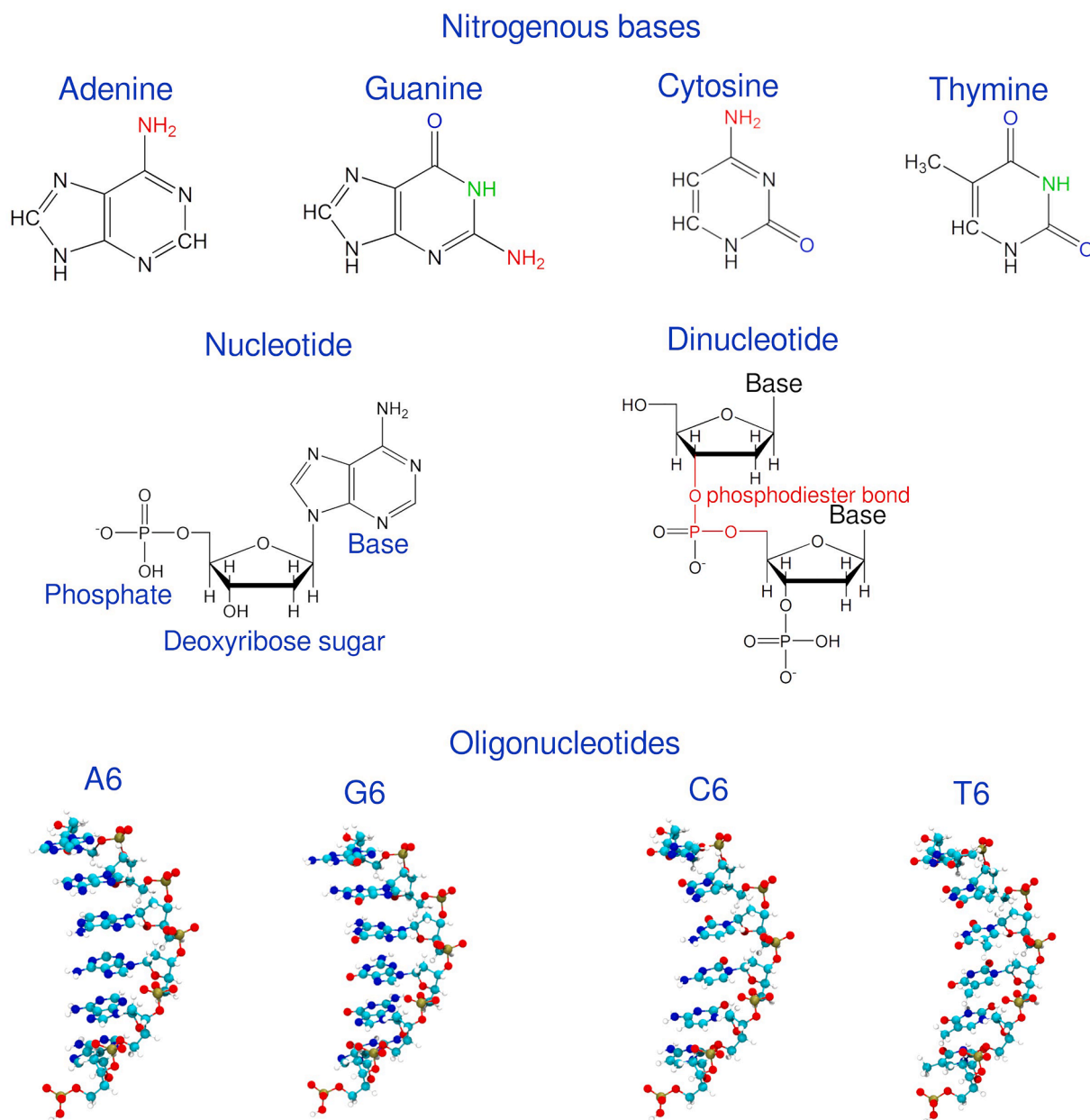


**Fig. 1.** Top: Chemical structures of nitrogenous bases. Middle: Chemical structure of nucleotide and a dinucleotide, showing the components of a nucleotide and the phosphodiester bond formed by the condensation reaction of two nucleotides, respectively. Down: Initial structures of A6, G6, C6 and T6 ssDNA segment used in the MD simulations. Color codes: red (O atoms), cyan (C atoms), blue (N atoms), white (H atoms), brown (P atoms).

[19] the authors show that nucleotides adsorb more strongly on TiO<sub>2</sub> surfaces at lower pH than at higher pH values. The nucleotides bind directly to the surface via the phosphate group, but different surface coverages and adsorption rates implies different surface interactions of nucleobases with the surface [19].

Despite these advancements, the computational exploration of oligonucleotide interactions on TiO<sub>2</sub> surfaces remains underexplored. Previous studies, on rutile (110) surface, using Density Functional based Tight Binding (DFTB) calculations (with cytidine monophosphate as adsorbate) [21] and classical molecular dynamics (MD) simulations, to examine the adsorption of single DNA bases [22], have begun to investigate these interactions, but significant gaps still remain. In a previous work, we studied nucleotide and dinucleotide adsorption on the anatase (101) surface using hybrid density functional theory (DFT) [23], highlighting, for the first time, the collaborative adsorption mode of phosphate anions and nucleobases. However, to the best of our

knowledge, larger oligonucleotides have not been investigated so far. In addition, it is worth mentioning that the anatase is the most common and stable phase of TiO<sub>2</sub> nanomaterials below 15 nm, being the face (101) frequently exposed by anatase nanocrystals, including natural samples [24].

In this article, we investigate the complex interactions between single-stranded DNA (ssDNA) fragments and TiO<sub>2</sub> surfaces at the atomic/molecular scale. Building on our prior density functional theory (DFT) study [23], we employ classical molecular dynamics (MD) simulations to investigate the adsorption mechanisms of ssDNA segments on the TiO<sub>2</sub> anatase (101) surface. The initial analysis considers four different ssDNA segments, each consisting of six identical nucleotide sequences: Adenine (A6), Guanine (G6), Cytosine (C6), and Thymine (T6). Key descriptors, including surface contact area, distance to the surface, hydrogen bonding and non-bonded interactions analysis, were employed to elucidate the adsorption behavior. Our findings reveal

different interaction levels, with A6 showing the highest degree of interaction with the surface, while T6 shows the lowest. The adsorption mechanism is driven by a dynamic cooperation between hydrogen bonding and phosphate group interactions with the surface, facilitating the ssDNA adsorption. In a further step, we explore the influence of ssDNA segment length by conducting additional simulations with longer oligonucleotides composed of either twelve Adenine (A12) or twelve Thymine (T12) nucleobases. Our results indicate that longer segments have a lower number of nucleobases interacting with the surface compared to shorter segments, highlighting the impact of segment length on adsorption behavior.

Moreover, to gain insights into how physiological conditions affect oligonucleotides adsorption mode and strength on TiO<sub>2</sub> surfaces, we also compare results for the neutral TiO<sub>2</sub> surface model, which mimics acidic conditions, with those for a negatively charged one, which mimics pH conditions around 7, for all short ssDNA segments. We wish to stress that, unlike prior DFTB or DFT studies [21–23], the current MD simulations include the effects of explicit water, salt, and temperature, making the findings more applicable to real-world biological and environmental conditions.

By providing a comprehensive atomic-scale analysis and exploring various factors influencing ssDNA-TiO<sub>2</sub> interactions, our study contributes to the fundamental understanding of the underlying mechanisms in these bioinorganic nanoconjugates, whose control may pave the way to more effective and novel applications in biosensing and gene therapy.

## 2. Theoretical and computational methods

### 2.1. Simulation protocol

In this work, all the classical MD simulations were carried out utilizing the Large-scale Atomic/Molecular Massively Parallel Simulator (LAMMPS) open-source code (version 24 Mar 2022) [25]. The TiO<sub>2</sub> anatase (101) surface was described by the Matsui and Akaogi's [26] empirical potential for Ti and O atoms, recently systematically verified by some of us for describing TiO<sub>2</sub>/organic interfaces [27], combined with the Lennard-Jones (12–6) parameters reported by Luan et al. [28] (See Supplementary Material for details of the Matsui and Akaogi's Force Field). The bonded and non-bonded parameters for the ssDNA molecules were assigned using the CHARMM36 force field [29] and the CHARMM-modified rigid TIP3P for the water molecules [30]. The TiO<sub>2</sub>/ssDNA topologies were generated using the MOLTEMPLATE [31] package.

Starting-point molecular structures for the ssDNA segments were built using the Avogadro package [32] and their corresponding molecular topology and FF parameters assigned using the PDB Reader & Manipulator module in the CHARMM-GUI webserver [33]. Fig. 1 shows the chemical structure of the nucleobases and that of a generic nucleotide, which consists of a nucleobase, a deoxyribose sugar, and a phosphate group. At physiological pH, each nucleotide carries a negative net charge due to the phosphate group. The condensation reaction of two nucleotides results in the formation of a phosphodiester bond, preserving the phosphate's net charge (−1), meaning that a ssDNA oligonucleotide has one negative charge per nucleotide. The simulations were conducted for four different ssDNA chains, each composed of six units of the same nucleotide (see Fig. 1), named A6, G6, C6 and T6. To ensure the system's electroneutrality, the negative charges were compensated by adding the appropriate number of potassium (K<sup>+</sup>) counter-ions in the simulation box. Either Na<sup>+</sup> or K<sup>+</sup> ions were used in previous MD simulations of ssDNA with solid surfaces [34,35]. Na<sup>+</sup> was reported to have a higher affinity for the DNA phosphate backbone [36], leading to a more compact DNA structure [37]. Based on this, we chose to use K<sup>+</sup> to prevent ssDNA collapse and to ensure improved interaction of the DNA oligomer with the surface. Additional calculations were performed using 12 nucleotide units (Fig. S1).

For the TiO<sub>2</sub> surface, a slab consisting of 768 TiO<sub>2</sub> units (three

triatomic layers) was placed in a simulation box with three-dimensional periodic boundary conditions, and dimensions of 60.83 × 41.92 × 110 Å (Fig. S2). The box size in the X and Y directions is defined by the slab length and width, making the slab periodic in those directions. In the first set of calculations, the surface was neutral (zero net charge). In the second set of calculations, we examined the effect of surface charge on the ssDNA adsorption process. To do so, we used the same slab with a slightly modification of the O<sub>2c</sub> surface atoms' charge to implicitly represent a surface charge density of −0.62 e/nm<sup>2</sup> [38], mimicking that found in experimental measurements for TiO<sub>2</sub> nanoparticles under neutral pH conditions [39–41]. In this case, additional K<sup>+</sup> counter-ions were added to maintain an electroneutral system. For the calculation using ssDNA segment of twelve units, the simulation box was increased to 91.24 × 62.56 × 110 Å.

In all cases, the simulation boxes were filled with water molecules at the experimental density of ~0.99 g/cm<sup>3</sup> using the PACKMOL [42] software, and the salt concentration was fixed at 0.15 M KCl. During all atomistic MD simulations, the positions of atoms within the TiO<sub>2</sub> slab were kept fixed, while the atoms of the ssDNA molecules, solvent molecules, and ions were free to evolve over time at 303 K (NVT ensemble). The integration of the Newton's equations of motion used a 2fs timestep, with the SHAKE algorithm [43] employed to impose holonomic constraints on all the covalent bonds involving hydrogen atoms in both water and ssDNA. The long-range solver Particle-Particle-Mesh (P3M) handled the electrostatic interactions with a real-space cut-off of 12.0 Å and a threshold of 10<sup>−5</sup> for error tolerance in forces [44]. The Lennard-Jones (12–6) interactions were truncated with a 10.0 Å cut-off distance. A minimization phase was carried out to minimize the potential energy of the system and ensure no overlaps between the atoms, followed by a 1 ns equilibration phase. Finally, the production phase explored 300 ns of the phase space in the NVT ensemble at 303 K. The visualization of the simulation trajectories was done using Visual Molecular Dynamics (VMD) [45].

### 2.2. Simulation analysis

The contact surface area (CSA) is defined as half the difference between the sum of the solvent-accessible surface areas (SASA) of the DNA molecule and the TiO<sub>2</sub> surface, and the SASA of the TiO<sub>2</sub>/ssDNA complex, as shown in the formula below,

$$\frac{(SASA_{ssDNA} + SASA_{TiO_2}) - SASA_{ssDNA/TiO_2}}{2}$$

Average interatomic distances. For all the systems we analyzed:

- the normal distance between the ssDNA center of mass (COM) and the TiO<sub>2</sub> surface.
- the end-to-end distance of the ssDNA segment,  $\langle h^2 \rangle^{1/2}_{ssDNA}$ , i.e. the mean distance between the center-of-mass of the first and the last nucleotide of each ssDNA segment.

The hydrogen bonds (H-bonds) analysis was carried out using the Hydrogen Bonds tool [45] implemented in VMD. We counted as an H-bond formation when these two criteria were satisfied: I) the distance between H-bond donor and the H-acceptor was less than 3.5 Å; II) the supplementary angle to the one formed between the H-donor and H-acceptor heavy atoms, having the hydrogen atom as the vertex, was less than 30°.

The non-bonded interaction energy was evaluated re-running the MD simulations trajectories and calculating the desired intermolecular interaction energies using the USER-TALLY package implemented in LAMMPS.

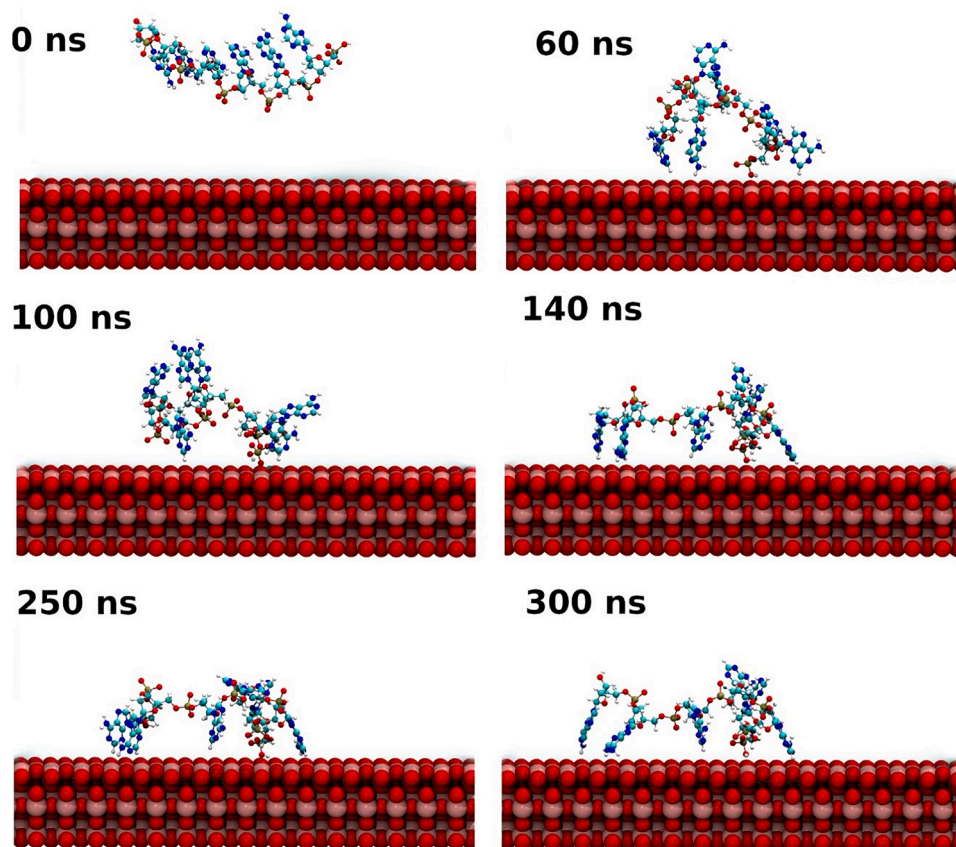


**Fig. 2.** Representative snapshots of the adsorption process evolution of the A6 ssDNA segment on the  $\text{TiO}_2$  anatase (101) surface over the 300 ns MD trajectory. Water molecules are not shown for clarity.

### 3. Results

#### 3.1. Mechanism of approach to and adsorption on $\text{TiO}_2$ anatase (101) by ssDNA segments

In this section, we present a comprehensive comparison of the adsorption processes for four distinct ssDNA oligonucleotides, each consisting of the same nucleobases, on the anatase (101) surface. To achieve this, we initially positioned the ssDNA 15 Å away from the surface and conducted simulations for each sample over a 300 ns long simulation time. The choice of a 15 Å distance from the surface was based on previous MD simulations of ssDNA adsorption on various surfaces, including hydrophobic, hydrophilic, and graphene oxide surfaces [46–49]. Also, considering the typical diffusion coefficient of ssDNA in water, which ranges between  $1 \times 10^{-6}$  and  $2 \times 10^{-6} \text{ cm}^2/\text{s}$  [50] depending on factors such as ssDNA length and ionic strength, a distance of 15 Å is optimal for observing the DNA approaching the surface and the subsequent adsorption process within the 300 ns timeframe of our simulations. These simulations offer a detailed atomic-level description of the intermolecular interactions between the ssDNA segments and the  $\text{TiO}_2$  surface.

To effectively monitor the adsorption process, we assess two key parameters: the normal distance between the center-of-mass (COM) of the ssDNA and the anatase (101) surface, and the CSA. Through these parameters, we gain valuable atomistic insights into the dynamics of the ssDNA segments as they adsorb onto the  $\text{TiO}_2$  surface.

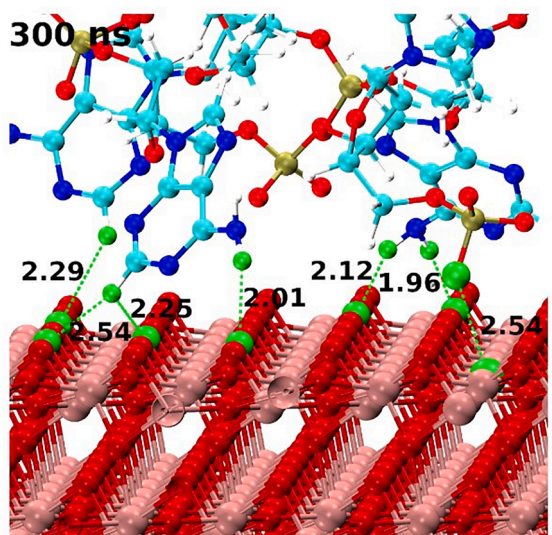
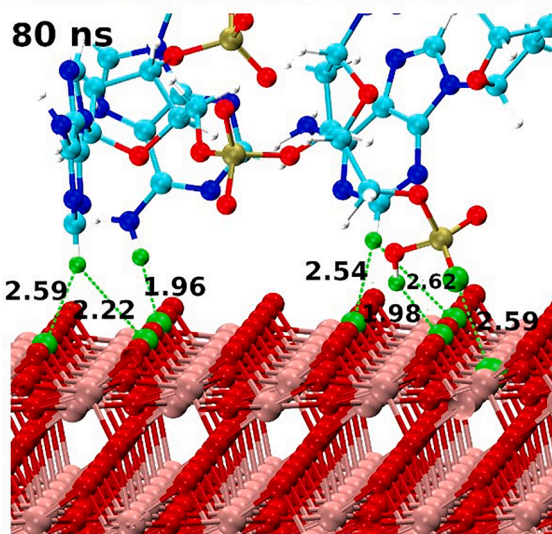
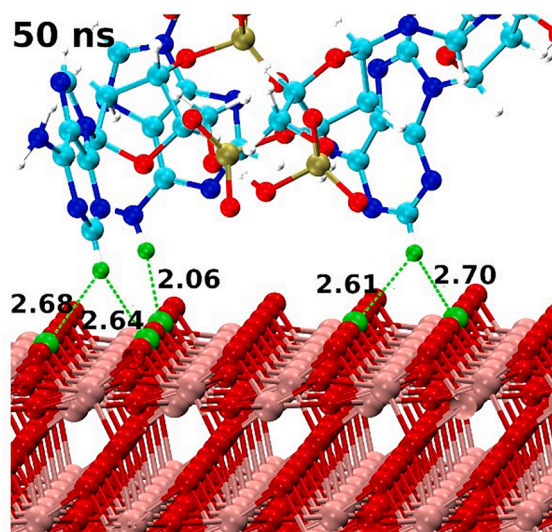
Moreover, we investigate the specific details of the primary interactions between the oligonucleotides and the  $\text{TiO}_2$  surface, shedding light on the underlying mechanisms driving the adsorption phenomenon.

Fig. 2 illustrates the progressive evolution of the A6 ssDNA segment

during different simulation times. As mentioned earlier, the simulation starts with the segment positioned at an average distance of approximately 15 Å away from the anatase surface. Along the simulation progress, we observed the segment gradually approaching the anatase surface. Notably, the initial interaction between the ssDNA and the surface occurred through the nucleobases. At the 50 ns, three nucleobases were observed perpendicular to the surface, actively interacting with it. Subsequently, between 60 ns and 100 ns, the terminal phosphate group of the ssDNA segment anchored firmly to the surface. Furthermore, at 140 ns, two additional nucleobases established interactions with the anatase surface, stabilizing the adsorption process. During the remaining duration of the simulation, the overall structure of the ssDNA segment remained practically unchanged.

In Fig. 3, we present the key intermolecular interactions between the nucleobases and the surface. Initially, after 50 ns, the formation of two types of hydrogen bonds is observed. One involves the amine group of an adenine with a surface  $\text{O}_{2c}$  atom, at an average distance of 2.06 Å. Additionally, we observe an interaction between an aromatic CH group of the nucleobase and an  $\text{O}_{2c}$  surface atom, with an average distance of 2.60 Å. This type of CH–O interaction is referred by some authors as a nonconventional or weak hydrogen bond interactions [51–54]. These nonconventional H-bond interactions demonstrate a preference for nonlinear interactions between nucleic bases and acceptor entities [51, 52], playing a significant role in molecular recognition within biological systems [53,54]. At 80 ns, a robust interaction between the terminal phosphate group and the anatase surface is observed through O– $\text{Ti}_{5c}$  bonding, with an average distance of 2.54 Å. This indicates the formation of a stable interatomic interaction that persists throughout the simulation until 300 ns. Furthermore, from 140 ns until the end of the simulation, new H-bonds interactions are formed involving the amine groups and the aromatic CH entities with the  $\text{O}_{2c}$  surface atoms. Fig. 3 at





**Fig. 3.** Representative snapshots of the adsorption process evolution of A6 ssDNA segment, highlighting the main interactions between the ssDNA components and the  $\text{TiO}_2$  anatase (101) surface. The water molecules are not shown for clarity.

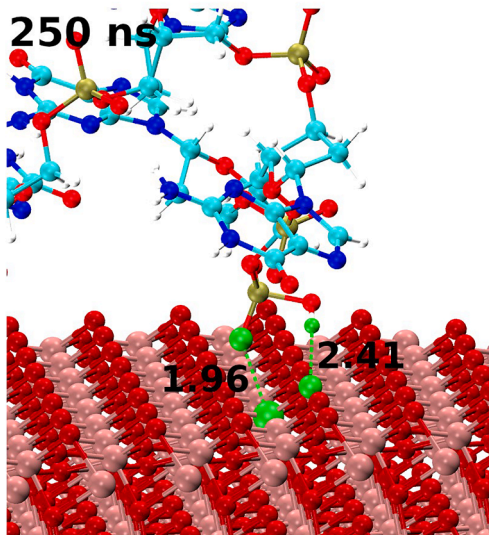
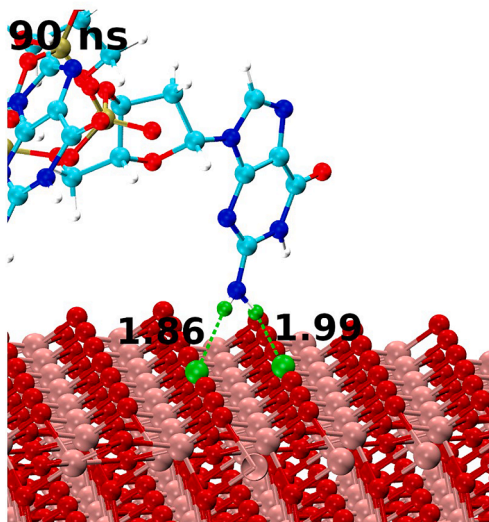
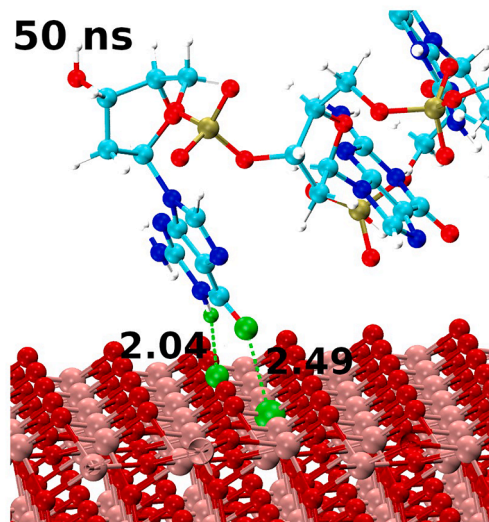


**Fig. 4.** Representative snapshots of the adsorption process evolution of G6 ssDNA segment, highlighting the main interactions between the ssDNA components and the  $\text{TiO}_2$  anatase (101) surface. The water molecules are not shown for clarity.

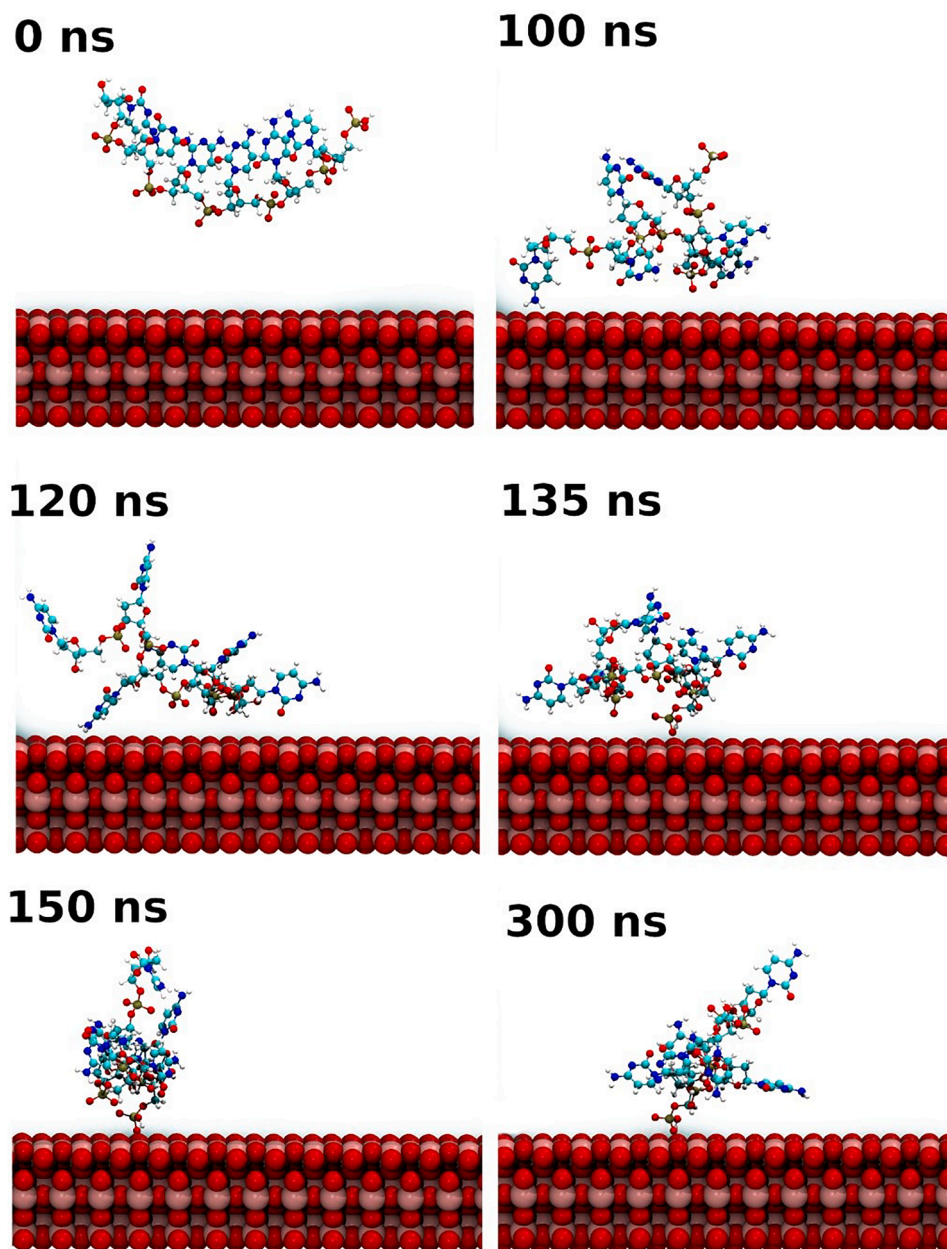


**Fig. 5.** Representative snapshots of the adsorption process evolution of C6 ssDNA segment on the  $\text{TiO}_2$  anatase (101) surface over the 300 ns long MD simulation trajectory.

300 ns shows how the amine group can simultaneously form two H-bonds with two different  $\text{O}_{2c}$  surface atoms.

Figs. 2 and 3 collectively underscore the vital role of nucleobases in the ssDNA adsorption process on the anatase (101) surface. The analysis of the other segments studied reveals both similarities and differences in the underlying mechanisms. In all cases, the initial interaction between the ssDNA segment and the surface originates from the nucleobases. However, these specific types of initial interactions vary across the segments.

In the case of G6, our findings reveal that the initial interaction between the ssDNA and the surface occurs at 50 ns of simulation time. This interaction, between a carbonyl oxygen (O) atom of a nucleobase and a  $\text{Ti}_{5c}$  site on the surface, is strong and accompanied by an H-bond involving the same nucleobase (as depicted in Fig. 4). Subsequently, at 90 ns, we observe the formation of two H-bonds. Finally, at 250 ns, the terminal phosphate interaction ( $\text{O}(\text{P})\text{-Ti}_{5c}$ ) is observed. Notably, the initial interaction, involving the carbonyl oxygen atom and the  $\text{Ti}_{5c}$  site,

persists throughout the entire simulation. This behavior can be attributed to the high adsorption energy associated with this specific adsorption mode, as previously determined by DFT calculations [23]. A comprehensive representation of the entire simulation is available in Fig. S3.

In the case of C6 (Fig. 5), the initial interaction between the ssDNA segment and the surface occurs at 100 ns of simulation time. It is worth noting that the time required for the initial interactions with the  $\text{TiO}_2$  surface is twice as long for C6 than for G6, suggesting a faster self-diffusion of the latter compared to the former. To confirm this assumption, we compare in Fig. S4 the linear regression of the Mean Squared Displacement (MSD) in the earlier stage of the simulation for C6 vs G6. From this data, it is evident that G6 presents a steeper slope compared to C6, indicating a faster diffusion of G6 than C6 in solution, which is the reason why G6 reaches the  $\text{TiO}_2$  surface more quickly than C6. The interaction of C6 with the surface involves the formation of an H-bond between the amine group of a nucleobase and a surface  $\text{O}_{2c}$



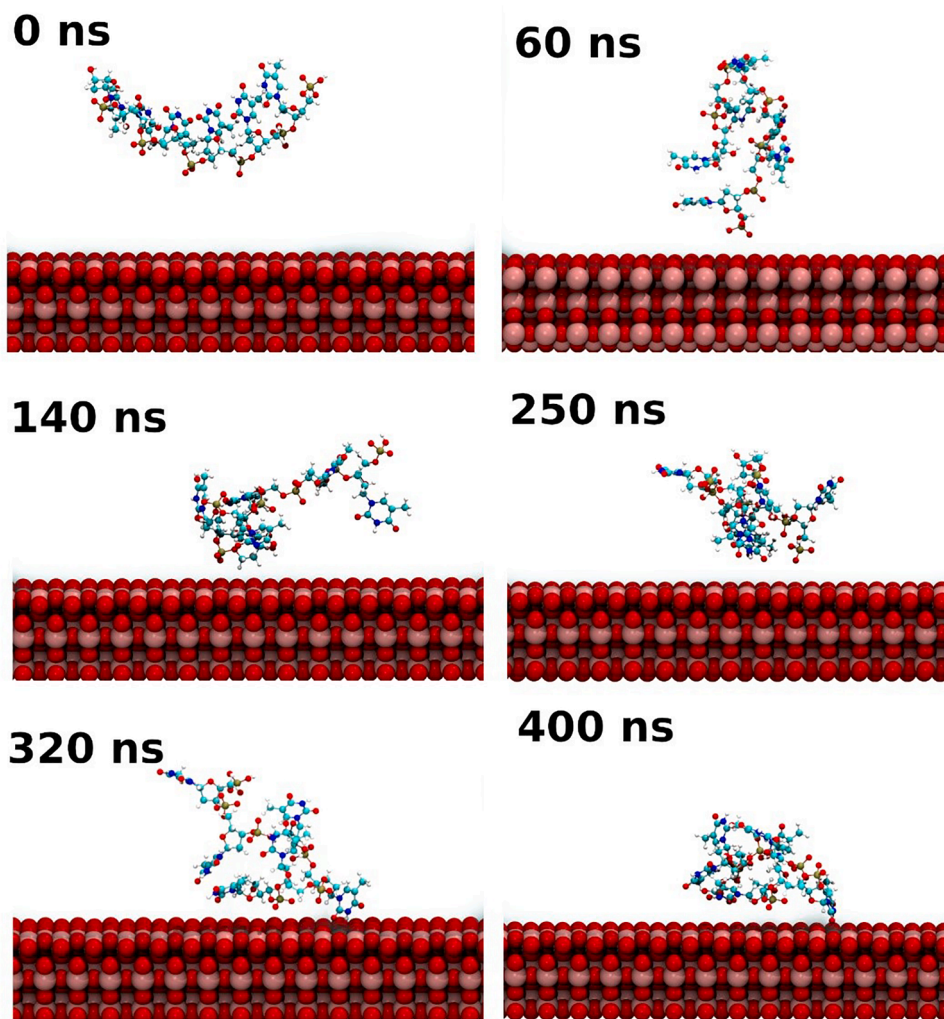


**Fig. 6.** Representative snapshots of the adsorption process of the T6 ssDNA segment on the TiO<sub>2</sub> anatase (101) surface over 400 ns long simulation trajectory. Water molecules are not shown for clarity.

atom. At 150 ns, a strong interaction between the terminal phosphate group and the surface is observed via an intermolecular O(P)-Ti<sub>5c</sub> interaction, which remains stable up to 300 ns of simulation time.

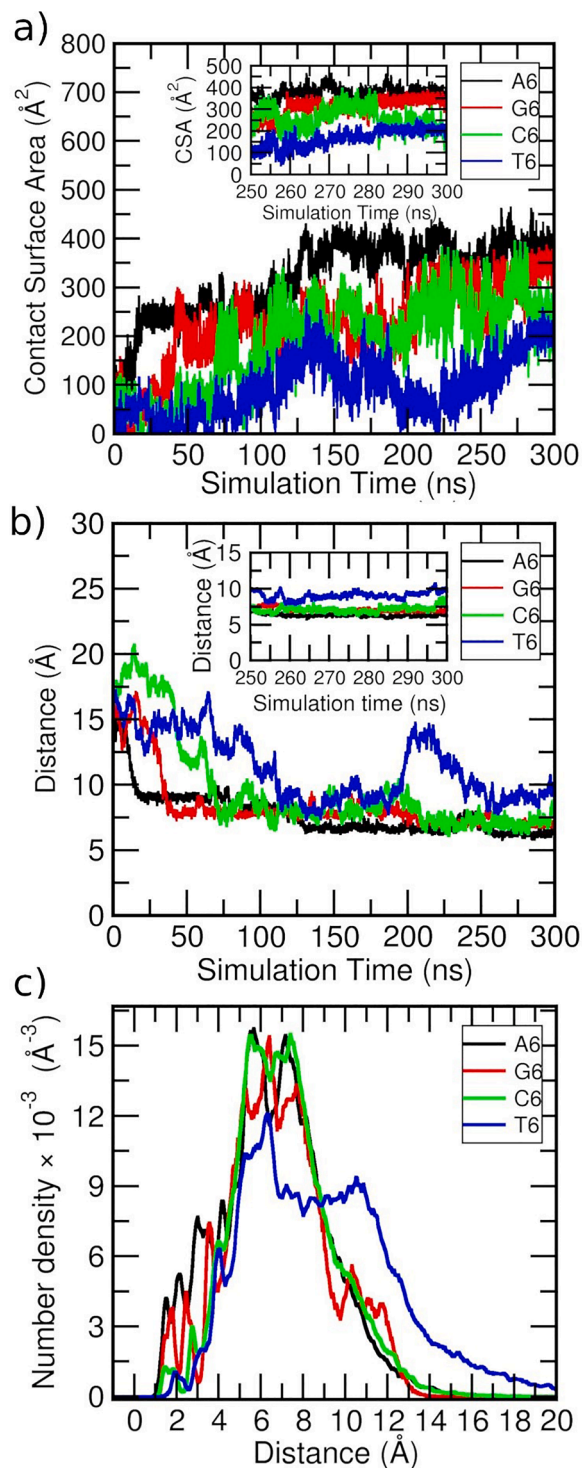
Finally, in the case of the T6 (Fig. 6), we observed the segment approaching the surface; however, a collaborative adsorption process involving both nucleobases and the phosphate group with the surface was not evident. Instead, specific interactions of the nucleobases or phosphate entity with the surface were observed during the simulation, but in an isolated manner. Even after extending the simulation to 400 ns, no clear attachment was observed, as specific interactions, such as H-bonds, phosphate interactions, or carbonyl interactions, formed and broke intermittently. It is plausible that the collaborative adsorption process for T6 may require more time to develop compared to the other segments, potentially due to its unique nucleobase composition and structural characteristics.

Fig. 7a presents the distance between the COM of each ssDNA segment and the surface. Initially, all segments begin at an average distance of around 15 Å away from the surface and gradually decrease during the first 125 ns of the simulation. Afterwards, the distance stabilizes and oscillates around a constant value. In the last 50 ns (inset in Fig. 7a), the distance remains almost constant. The average distance values for each segment in the last 50 ns are provided in Table I. A6 has the shortest distance ( $6.57 \pm 0.42$  Å) to the anatase (101) surface, followed by G6, C6, and T6, respectively. The decrease in distance correlates with an increase in the CSA of each segment, as shown in Fig. 7b.

During the first 125 ns, all ssDNA segments show an increase in CSA. Subsequently, A6, C6, and G6 maintain a constant CSA, while T6 exhibits higher oscillations, likely due to the absence of specific interactions with the surface. Notably, there is a clear correlation between the COM distance and CSA for T6. An increase in the normal distance between 175 and 250 ns corresponds to a decrease in CSA during the same simulation timeframe. In the last 50 ns, the CSA remains nearly constant for each segment. A6 demonstrates the highest contact area with the surface, followed by G6, C6, and T6, respectively.

Experimental results show that the adsorption of single nucleotides on TiO<sub>2</sub> nanoparticles is primary driven by phosphate adsorption, with the adsorption trend being ADE > GUA > CIT > THY [19]. For larger oligonucleotides, experimental reports indicate similar adsorption capacities for adenine and cytosine, while guanine shows slightly lower adsorption, and thymine exhibits the lowest adsorption capacity [17]. These results are consistent with our findings. As shown in Figs. 7a and 7b, thymine has the lowest CSA and the highest average distance with the surface indicating a weaker interaction with it. Adenine has the highest CSA and shortest distance to the surface, while Guanine and Cytosine have an intermediate behavior.

Fig. 7c displays the number density profiles for each ssDNA segment during the last 100 ns of the simulation. For A6, G6, and C6, the profiles show maximum intensity between 5–8 Å from the surface, with density extending up to ~15 Å. In contrast, the profile for T6 differs from the others, with a peak at around 6 Å (with lower intensity), followed by a



**Fig. 7.** Evolution of different parameters over the 300 ns of simulation time for the adsorption process of ssDNA on the anatase (101) surface: a) Contact surface area (CSA). b) Distance between the ssDNA COM and the surface. c) Number density profile of ssDNA segments along the  $z$ -axis over the last 100 ns of simulation.

plateau extending until 11 Å, and then stretching up to ~22 Å. The analysis of the profiles indicates that during the simulation, T6 remains farther from the surface compared to the other segments.

Furthermore, well-defined peaks between 1.5 and 3.5 Å are observed in all cases, attributed to the formation of stable H-bonds and O(P)-Ti interactions. Interestingly, in all segments, only the terminal

**Table I**

Average values of CSA and COM distance calculated over the last 50 ns for each ssDNA segment. Simulation started with the ssDNA at least 15 Å away from the surface.

	CSA (Å <sup>2</sup> )	COM distance (Å)
A6	369.5 ± 26.6	6.57 ± 0.42
G6	314.0 ± 33.3	7.01 ± 0.22
C6	257.6 ± 47.3	7.24 ± 0.53
T6	134.7 ± 61.0	8.57 ± 0.84

phosphate group interacts with the surface, while the rest of the phosphate groups remain away from the surface.

### 3.2. Interaction of oligonucleotides with the TiO<sub>2</sub> surface through the phosphate group

In this section, we carried out a new set of calculations, starting the simulations with the oligonucleotide's terminal phosphate group already interacting with the anatase surface (see Fig. S5). The primary aim was to investigate whether this different starting point configuration would alter the observed behaviors from the previous section.

Throughout the entire simulation, we noted that the phosphate group consistently remained attached to the surface. The analysis of the CSA yielded the same trend as observed when starting the simulations with the ssDNA segments positioned 15 Å away from the surface. Fig. 8a illustrates a decrease in the distance between the COM of each ssDNA segment and the surface during the first 150 ns, followed by a relatively constant distance for each segment. As before, the decrease in COM distance corresponds to an increase in CSA during the initial 150 ns (Fig. 8b). Subsequently, the CSA remains almost constant for each segment, consistent with the previous findings. Table II summarizes the average CSA and COM distance values for the last 50 ns of the simulation, displaying the same absorption trend as in Table I: A6 > G6 > C6 > T6.

To gain further insights into the orientation and affinity of the nucleobases to the surface, we calculated the average angle formed between the ssDNA segment and the surface during the simulation. An angle of 90° indicates an upright configuration of the segments, while an angle of 0° denotes a parallel alignment with the surface. Fig. 8c depicts the variation of the angle during the first 100 ns, followed by a stabilization at around 150 ns for each ssDNA segment. The inset shows the last 50 ns of the simulation. Specifically, the average angle for A6 is 10.84°, while for T6, it reaches 25.71°, the highest value among the nucleobases. G6 and C6 fall in between, with angles of 13.27 and 15.88°, respectively. These results clearly demonstrate that T6 nucleobases exhibit the lowest affinity for the surface, whereas A6 nucleobases display a stronger interaction due to their lower angle.

### 3.3. Comparison of the MD results with previous DFT calculations

In the investigation of biomolecule-surfaces interactions using classical molecular mechanics MD methods, validating the accuracy of these simulations against higher-level calculations is a critical step to ensure reliable outcomes.

In a previous work, we meticulously investigated the adsorption of both single and dinucleotides on the anatase (101) surface using dispersion-corrected hybrid DFT calculations [23]. Analyzing the adsorption energies was crucial for uncovering a collaborative and synergistic adsorption mode. Specifically, our findings indicated that guanine-based nucleotides exhibited the highest adsorption strengths, while thymine-based nucleotides displayed the lowest. Adenine and cytosine-based nucleotides fell in between, offering insights into the varying affinities of different nucleotide components with the surface. In more detail, the phosphate anion forms a stable O-Ti interaction with the surface, while nucleobases engage in various interactions depending on



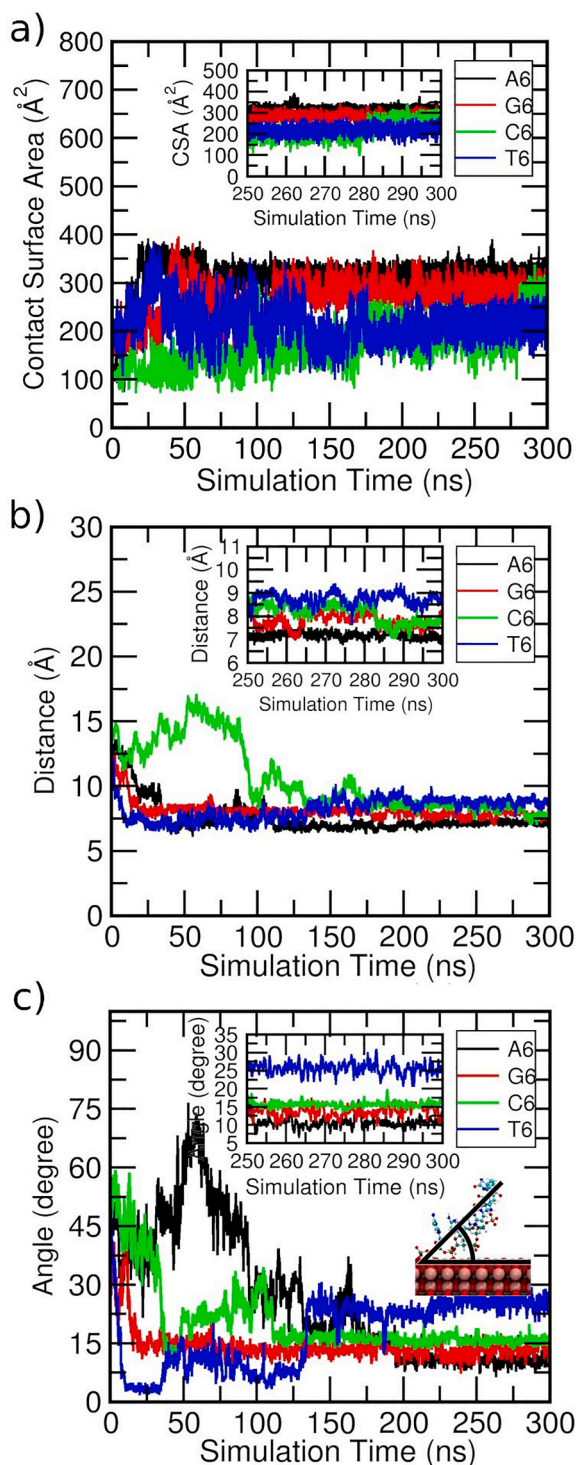


**Fig. 8.** Evolution of different parameters over the entire 300 ns long simulation when it starts with the terminal phosphate group on the surface: a) Contact surface area (CSA). b) Distance of the ssDNA COM and the surface. c) Average angle formed between the ssDNA and the surface during the simulation. The insets show the last 50 ns of simulation.

their structural features. Specifically, H-bond formations between the amine groups of nucleobases and  $O_{2c}$  atoms of the surface were observed, along with the creation of a stable interaction between the carbonyl group of the nucleobases and the  $Ti_{5c}$  surface atom.

In our current MD study, comparisons with our earlier DFT calculations confirm the accuracy of our simulation outcomes. The analogous

**Table II**

Average values of CSA, COM distance and surface-segment angle calculated over the last 50 ns of simulation time for each ssDNA segment. Simulation started with the ssDNA interacting with the surface through its terminal phosphate group.

	CSA (Å <sup>2</sup> )	COM distance (Å)	Angle with the surface (degree)
A6	317.4 ± 14.1	7.15 ± 0.14	10.84 ± 1.43
G6	284.6 ± 15.5	7.79 ± 0.26	13.27 ± 1.73
C6	242.6 ± 34.2	8.21 ± 0.37	15.88 ± 0.91
T6	222.2 ± 31.6	8.56 ± 0.28	25.71 ± 1.66

interactions between single-stranded DNA (ssDNA) segments and the  $TiO_2$  surface in the DFT calculations further emphasize the robustness of our classical findings. Regardless of the nucleobases involved, our MD simulations consistently highlight the interaction of the terminal phosphate anion, which is sustained by recurrent and stable O-Ti interactions.

Furthermore, the MD simulations reveal additional details, displaying similar characteristics as the DFT calculations: H-bond formations involving  $NH_2$  and  $NH$  groups, as well as the formation of stable interactions between carbonyl groups and Ti surface atoms (specifically observed for G6, C6, and T6). In addition, the present simulation shows the formation of stable nonbonded interactions between the CH group and the  $O_{2c}$  surface atom. Overall, this validation step not only reinforces the accuracy of our MD simulation outcomes but also expands our understanding of the intricate biomolecular interactions at the atomistic/molecular level.

#### 3.4. Evolution of the nonbonded interactions during the MD simulations

To quantify, from an energetic point of view, the role of nonbonded interactions in the adsorption process of the ssDNA on the  $TiO_2$  surface, we separately evaluate the electrostatic and vdW interactions that constitute the total intermolecular interaction energy, as well as the H-bonds established between them.

We observe that vdW interactions mainly govern the adsorption process. In all cases we see a correlation between the CSA plots and the vdW interaction energy as a function of simulation time, as shown in Fig. 9. A reduction in the vdW energies values (left axes, black curves,) are followed by an increase in the CSA (right axes, red curves), while a reduction of the CSA implies an increase in the vdW energies. When the CSA remains constant, the vdW energy does too. Even more, the energy oscillations align with the oscillations in the CSA. This behavior is consistent across different ssDNA chains and independent of the starting point configuration. For instance, when the ssDNA is 15 Å away from the surface (Fig. S6), the initial vdW interaction energy is practically absent, while, when the terminal phosphate group of ssDNA is already interacting with the surface, the initial vdW interaction energy is already about  $-10$  kcal/mol.

Table III summarizes the mean values and standard deviations for the non-bonded interactions over the last 50 ns of the simulation, starting with the ssDNA already interacting with the surface, along with the mean number and standard deviations of H-bonds formed during the same simulation time frame. The analysis of Table III indicates that vdW interactions for A6 and G6 are generally stronger (more negative values) than for C6 and T6, which agrees with the higher CSA values obtained for the former compared to the latter (see Tables II). A similar behavior is observed when the simulation starts with ssDNA segment at 15 Å from the surface (Table S1).

#### 3.5. Effect of the $TiO_2$ surface charge on the ssDNA adsorption

This section examines the impact of surface charge on the adsorption of the oligonucleotides. According to some experimental studies [39–41], the surface of  $TiO_2$  nanoparticles is negatively charged under neutral pH. In standard conditions, potentiometric studies of the

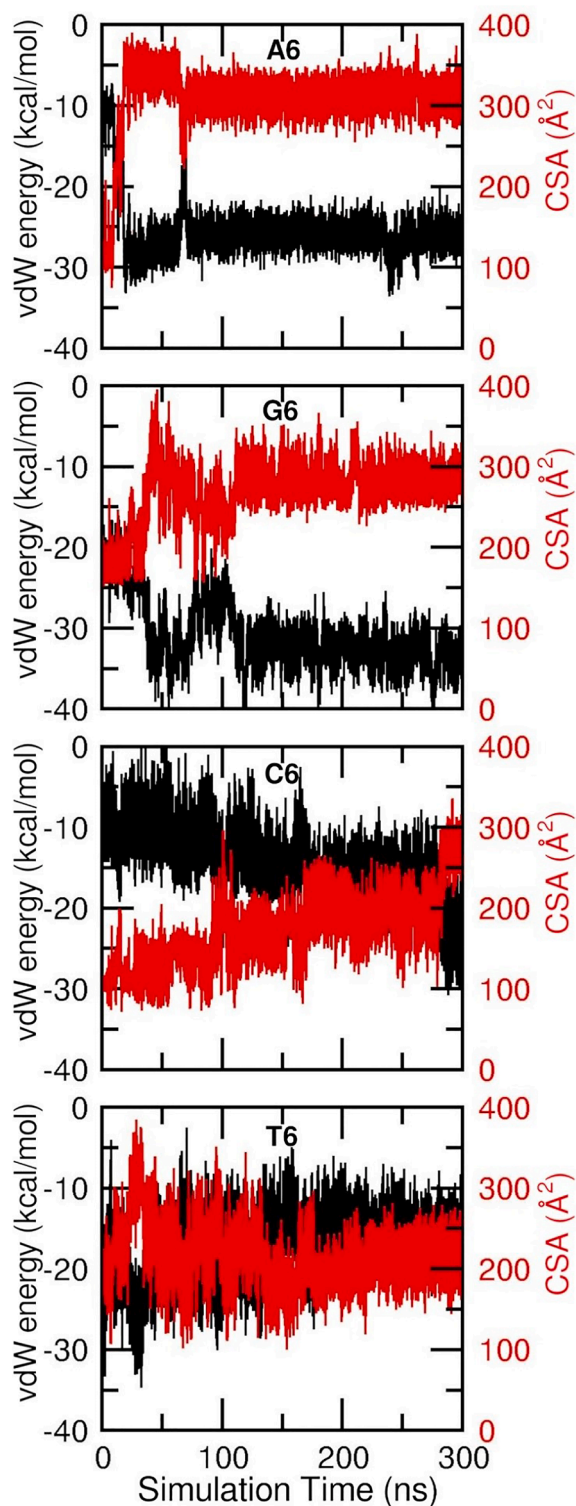


**Fig. 9.** Evolution of vdW interaction energy for A6, G6, C6, and T6 (black curves, left axis) contrasted with their corresponding CSA evolution (red curves, right axis). Simulation started with the ssDNA segment already interacting with the surface.

rutile-water interface [39] indicate that the surface charge density is about  $-0.62 \text{ e/nm}^2$ . Similarly,  $\text{TiO}_2$  nanoparticles comprising 80 % anatase and 20 % rutile exhibit a surface charge density of  $-0.56 \text{ e/nm}^2$  under analogous conditions [41]. The simulation starts with the oligonucleotide's terminal phosphate group near to the anatase surface. The progress of the CSA and the COM distance between the oligonucleotides

**Table III**

Average of non-bonded interaction energies and number of H-bonds between the ssDNA segments and the neutral surface calculated over the last 50 ns of simulation time starting with the ssDNA segments already interacting with the surface.

	vdW	Coulomb	# of H-bonds
A6	$-26.3 \pm 2.9$	$-15.3 \pm 2.8$	$3.5 \pm 0.8$
G6	$-33.3 \pm 3.2$	$2.9 \pm 1.4$	$2.1 \pm 0.3$
C6	$-19.1 \pm 3.3$	$24.4 \pm 4.5$	$0.9 \pm 0.4$
T6	$-17.6 \pm 3.5$	$3.4 \pm 3.2$	$0.8 \pm 0.4$

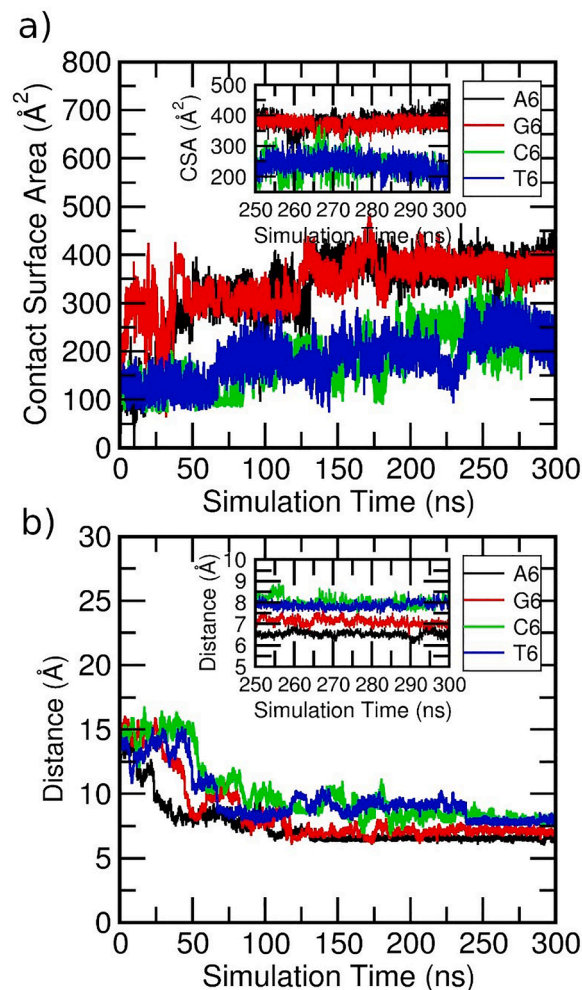


**Fig. 10.** Evolution of different parameters over the 300 ns of simulation time when it starts with the terminal phosphate group on the charged surface: a) Contact surface area (CSA). b) Distance of the ssDNA COM and the charged surface. The insets show the last 50 ns of simulation.

**Table IV**

Average of CSA and COM distance calculated over the last 50 ns of simulation time for each ssDNA segment for charged  $\text{TiO}_2$  surface.

	CSA ( $\text{\AA}^2$ )	COM distance ( $\text{\AA}$ )
A6	$394.6 \pm 26.5$	$6.46 \pm 0.16$
G6	$372.1 \pm 15.7$	$7.07 \pm 0.14$
C6	$241.4 \pm 29.6$	$7.94 \pm 0.22$
T6	$237.3 \pm 24.6$	$7.86 \pm 0.14$

and the charged surface are depicted in Fig. 10. Subsequently, two distinct behaviors are observed as shown in Fig. 10a. The oligonucleotides comprising purine bases (A6 and G6) manifest a higher affinity

**Table V**

Average of non-bonded interaction energies and number of H-bonds between the ssDNA segments and the charged surface calculated over the last 50 ns of simulation time.

	vdW	Coulomb	# of H-bonds
A6	$-37.6 \pm 2.9$	$-20.4 \pm 4.0$	$3.9 \pm 0.8$
G6	$-20.1 \pm 3.7$	$-26.6 \pm 6.4$	$3.6 \pm 0.8$
C6	$-23.9 \pm 4.6$	$18.1 \pm 10.6$	$1.6 \pm 0.8$
T6	$-18.8 \pm 3.8$	$10.5 \pm 7.1$	$0.6 \pm 0.5$

towards the  $\text{TiO}_2$  surface as compared to ssDNA composed by pyridine bases. The COM distance is significantly shorter for A6 and G6 in comparison to C6 and T6 (Table 4). Furthermore, the CSA values for purines are 24.3 % and 30.7 % higher for A6 and G6 (and COM distance lower) than those on a neutral surface, starting from the same starting point. This suggests a stronger interaction with the surface when it is negatively charged. For ssDNA composed of pyridine bases, a comparison of Tables 2 and 4 show that the values for CSA are comparable for both neutral ( $242.6 \pm 34.2$  and  $222.2 \pm 31.6 \text{ \AA}^2$  for C6 and T6) and charged ( $241.4 \pm 29.6$  and  $237.3 \pm 24.6 \text{ \AA}^2$  for C6 and T6)  $\text{TiO}_2$  surfaces, indicating lower influence on the adsorption of these bases when the surface is negatively charged.

Experimental studies have revealed a significant disparity in the interaction of single-stranded DNA (ssDNA) with  $\text{TiO}_2$  surface under varying pH conditions [17,18]. Specifically, at an acidic pH of 2, resulting in a positively charged surface, the amount of ssDNA adhering to the surface is considerably higher than at the physiological pH. This phenomenon can be attributed to the protonation of DNA bases at pH 2, causing only the negatively charged phosphate groups to interact with the surface, in an upright conformation. In contrast, at physiological pH, ssDNA wraps around the  $\text{TiO}_2$  NPs, indicating adsorption through the DNA bases as well [19]. Our results support these experimental findings.

Our simulations show that a negatively charged surface (physiological conditions) leads to greater interaction between DNA purines bases and the surface, resulting to higher CSA values compared to a neutral surface (slightly acidic conditions).

As for the neutral surface, we observe that the interaction between the oligonucleotides and the surface is mostly due to H-bonds,  $\text{CH}/\text{O}_{2c}$  interactions and the formation of stable interactions between carbonyl group and  $\text{Ti}_{5c}$  surface atom. We do not observe planar adsorption mode through  $\pi$ - $\pi$  interaction between the bases and the surface as observed in graphene and graphene oxide surfaces [47,48,55].

The analysis of the non-bonded interactions (Table 5) reveals a consistent trend with the neutral surface, where vdW interactions are favorable in all cases. Fig. S7 shows the existence of the same correlation between the CSA plots and vdW interaction energies as seen in the neutral surface. When examining electrostatic interactions, we find that for C6 and T6 segments, no discernible changes are observed compared to the neutral surface, indicating unfavorable interactions (reflected by the positive values). With respect to A6 and G6 segments, we observe an important increase in the electrostatic interactions, manifested by more negative values compared to the neutral surface. In addition, an increase in the average number of H-bonds (more pronounced for G6) is observed, indicating increased interaction with the charged surface. This increase in H-bonds can explain the corresponding increment in CSA and the subsequent reduction in the COM distance for A6 and G6 segments compared to the neutral surface.

To understand the differences in adsorption trends, we inspected the electrostatic potential surface (EPS) of each ssDNA segment using the APBS plugin [56]. Fig. S7 shows the EPS of each ssDNA segment in its initial configuration. The red regions represent areas of negative potential, primarily due to the phosphate groups, while the blue regions represent areas of positive potential. All segments show a predominant red region in the EPS. However, for purine ssDNA segments (A6 and G6), more distinct hotspots with high positive potentials (blue zones) are

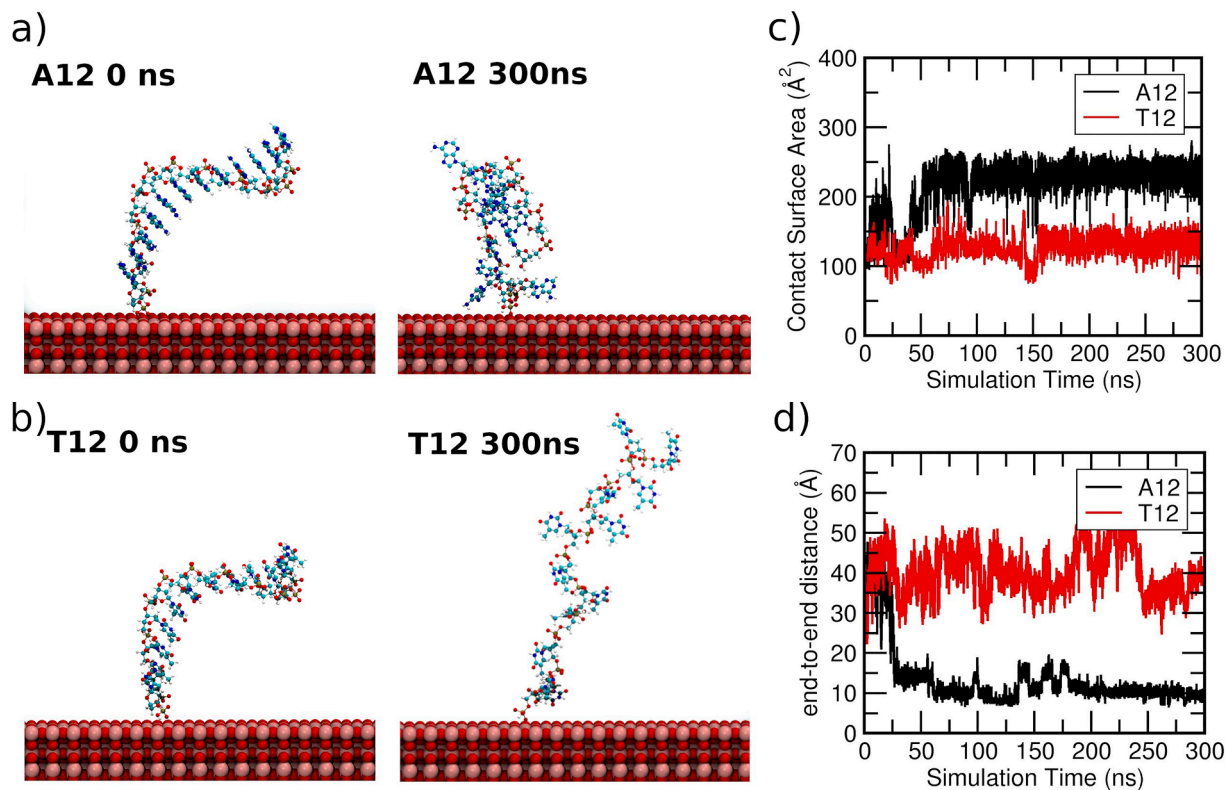


**Fig. 11.** Snapshots depicting the initial and final molecular conformations at 0 and 300 ns MD simulation time, respectively. a) A12 ssDNA segments and b) T12 ssDNA segments. Water molecules are not shown for clarity. c) and d) evolution during the simulation time of end-to-end distance of the ssDNA segments and the contact surface area of the ssDNA segments with the anatase (101) surface, respectively.



observed, mainly located on the nucleobases compared with the pyrimidine's ssDNA segments. Despite the overall negative charge of both the TiO<sub>2</sub> surface and the ssDNA segment, these regions of positive potential of the ssDNA nucleobases allow favorable interactions with the substrate.

Additionally, the Ti atoms on the TiO<sub>2</sub> surface are positively charged, which attract and anchor the negatively charged phosphate groups of the DNA. This interaction, driven by the localized positive charges on the Ti atoms, overcomes the repulsive forces between the negatively charged regions, facilitating the adsorption of DNA onto the TiO<sub>2</sub> surface. This interplay of local charges and electrostatic interactions is crucial for understanding the adsorption behavior observed in our simulations.

### 3.6. Effect of the length of the ssDNA

In this section, we conducted a set of simulations to investigate the adsorption behavior of ssDNA segments composed of twelve units of Adenine (A12) or Thymine (T12). These nucleobases were chosen because their six-unit oligonucleotides present the highest and lowest adsorption energy. The primary objective was to study the influence of ssDNA segment length on the adsorption strength. To simplify the study, we initiated the simulation directly with the ssDNA segment on the TiO<sub>2</sub> surface.

Fig. 11 shows the geometries at the start and end of the simulation for the A12 and T12 segments on the surface, together with the corresponding CSA plot and the distance between the first and last nucleotide in the ssDNA segment. During the simulation, we observed two different behaviors between the segments, as well as differences compared to the shorter segments.

For A12, in contrast to A6, only two nucleotides interacted with the surface. One nucleotide interacted through its phosphate group, while the other formed an H-bond with the amine group of an adenine base. This behavior contrasted with A6, where more nucleobases interacted with the surface. However, we also observed some  $\pi$ - $\pi$  stacking interactions between nucleobases in A12 (Fig. S9), which may explain the reduced interaction with the surface. Consequently, the CSA for A12 ( $234.7 \pm 11.9 \text{ \AA}^2$ ) was smaller than that for A6 ( $317.4 \pm 14.1 \text{ \AA}^2$ ), reflecting fewer bases interacting with the surface. Additionally, the A12 segment exhibited a wrapping behavior, folding around itself (see inset at 300 ns, Fig. 11a). On the other hand, T12 demonstrated minimal interaction of nucleobases with the surface. Only the nucleotide with the phosphate group initially displaced near to the surface remained in contact throughout the simulation, while the rest of the segment faced the solution (Fig. 11b). The CSA remained nearly constant throughout the simulation, with an average of  $131.6 \pm 15.1 \text{ \AA}^2$  in the last 50 ns. This value was even lower than that found for the T6 segment, indicating weaker nucleobase-surface interactions for T12.

Comparing A12 and T12, similar to A6 and T6, we observed higher CSA (see Fig. 11c) values for A12, indicating stronger interactions with the surface. Notably, T12 exhibited a larger distance between the first and last nucleotides compared to A12 (Fig. 11d), with an average value of  $36.2 \pm 3.1 \text{ \AA}$  for T12 and  $9.6 \pm 0.9 \text{ \AA}$  for A12 in the last 100 ns of simulation. This discrepancy may be due to the higher nucleobase affinity of the A12 segment for the surface, inducing a wrapping behavior not observed in T12 ssDNA.

## 4. Conclusions

In this work we have investigated which interactions determine the adsorption mechanism of ssDNA segments on TiO<sub>2</sub> anatase (101) surface at an atomic/molecular level using classical molecular dynamics simulations at realistic conditions of water solvation, ionic strength and temperature. This study provides significant insights for the understanding of DNA/TiO<sub>2</sub> nanoconjugates, filling a critical gap in theoretical investigations. Different key descriptors, such as surface contact

area, distance to the surface, hydrogen bond formation, and non-bonded interactions, are used in our analysis that also includes the effect of varying the DNA fragment length and pH conditions. We can summarize the most important findings as follows:

- 1. Dynamic cooperative adsorption:** The adsorption process begins with interactions between the DNA bases and the TiO<sub>2</sub> surface, facilitated by hydrogen bonds and interactions between the carbonyl oxygen of the nucleobase and surface Ti<sub>5c</sub> sites. Then, stable interactions are eventually established between the terminal phosphate group of the DNA segments and surface Ti<sub>5c</sub> atoms.
- 2. Sequence-dependent adsorption strength:** Adenine-based segments (6 units) exhibit the strongest adsorption, followed by Guanine, Cytosine, and Thymine. This sequence-dependent behavior is crucial for designing stable oligonucleotides/TiO<sub>2</sub> nanoconjugates.
- 3. ssDNA segment length effect:** ssDNA fragments of double length (12 units) for Adenine and Thymine are found to reduce their direct interaction with the surface and adopt a more vertical alignment compared to the shorter (6 unit) segments.
- 4. Surface charge (pH) effects:** Purine bases show higher affinity for the negatively charged TiO<sub>2</sub> surface, while pyrimidine bases exhibit similar adsorption whether the surface is negatively charged or neutral. This highlights the key role of pH conditions, which are those determining the actual TiO<sub>2</sub> surface charge, on the type and strength of DNA/TiO<sub>2</sub> interaction.

These findings align well with experimental data particularly with those obtained by fluorescence experiments [17] and ATR-FTIR spectroscopy [19], which show that at physiological pH (negatively charged surfaces) the purine nucleotides show higher adsorption and surface coverage compared to pyrimidine derivatives [19], while at acidic pH the interaction of the bases becomes less important and the interaction through the phosphate become preferentially with the oxide surface [17]. This study provides essential groundwork for the future design and development of advanced nanotechnological systems based on DNA-/TiO<sub>2</sub> nanoconjugates for biosensing and gene therapy.

## CRediT authorship contribution statement

**Federico A. Soria:** Writing – original draft, Visualization, Investigation, Formal analysis, Data curation. **Paulo Siani:** Writing – review & editing, Validation, Investigation, Formal analysis. **Cristiana Di Valentini:** Writing – review & editing, Supervision, Resources, Project administration, Funding acquisition, Formal analysis, Conceptualization.

## Declaration of competing interest

The authors declare that they have no known competing financial interests or personal relationships that could have appeared to influence the work reported in this paper.

## Data availability

Data will be made available on request.

## Acknowledgment

FAS acknowledges funding from Foncyt (PICT-2021-I-INVI-00812). Part of this work used computational resources from CCAD – Universidad Nacional de Córdoba (<http://ccad.unc.edu.ar/>), which is part of SNCAD – MinCyT, República Argentina.

The research leading to these results has received funding from the European Union - NextGenerationEU through the Italian Ministry of University and Research under PNRR - M4C2-I1.3 Project PE\_00000019



“HEAL ITALIA” to Prof. Cristiana Di Valentin CUP H43C22000830006 of University of Milano Bicocca.

## Supplementary materials

Supplementary material associated with this article can be found, in the online version, at [doi:10.1016/j.surf.2024.104889](https://doi.org/10.1016/j.surf.2024.104889).

## References

- [1] P.D. Howes, R. Chandrawati, M.M. Stevens, Colloidal nanoparticles as advanced biological sensors, *Science* (1979) 346 (2014) 1247390, <https://doi.org/10.1126/science.1247390>.
- [2] A. Samanta, I.L. Medintz, Nanoparticles and DNA – a powerful and growing functional combination in bionanotechnology, *Nanoscale* 8 (2016) 9037–9095, <https://doi.org/10.1039/C5NR08465B>.
- [3] J. Schneider, M. Matsuoka, M. Takeuchi, J. Zhang, Y. Horiuchi, M. Anpo, D. W. Bahnemann, Understanding TiO<sub>2</sub> Photocatalysis: mechanisms and Materials, *Chem. Rev.* 114 (2014) 9919–9986, <https://doi.org/10.1021/cr5001892>.
- [4] Y. Ma, X. Wang, Y. Jia, X. Chen, H. Han, C. Li, Titanium Dioxide-Based Nanomaterials for Photocatalytic Fuel Generations, *Chem. Rev.* 114 (2014) 9987–10043, <https://doi.org/10.1021/cr500008u>.
- [5] S. Shen, J. Chen, M. Wang, X. Sheng, X. Chen, X. Feng, S.S. Mao, Titanium dioxide nanostructures for photoelectrochemical applications, *Prog. Mater. Sci.* 98 (2018) 299–385, <https://doi.org/10.1016/j.pmatsci.2018.07.006>.
- [6] M. Bhogaita, S. Yadav, A.U. Bhanushali, A.A. Parsola, R.P. Nalini, Synthesis and characterization of TiO<sub>2</sub> thin films for DSSC prototype, *J. Photochem. Photobiol., A* 164 (2004) 2052–2061, <https://doi.org/10.1016/j.matpr.2016.04.108>.
- [7] Y. Bai, I. Mora-Seró, F. De Angelis, J. Bisquert, P. Wang, Titanium Dioxide Nanomaterials for Photovoltaic Applications, *Chem. Rev.* 114 (2014) 10095–10130, <https://doi.org/10.1021/cr400606n>.
- [8] U. Joost, A. Sutka, M. Oja, K. Smits, N. Döbelin, A. Loot, M. Järvekülg, M. Hirsimäki, M. Valden, E. Nömmiste, Reversible Photodoping of TiO<sub>2</sub> Nanoparticles for Photochromic Applications, *Chem. Mater.* 30 (2018) 8968–8974, <https://doi.org/10.1021/acs.chemmater.8b04813>.
- [9] T. Rajh, N.M. Dimitrijevic, M. Bissonnette, T. Koritarov, V. Konda, Titanium Dioxide in the Service of the Biomedical Revolution, *Chem. Rev.* 114 (2014) 10177–10216, <https://doi.org/10.1021/cr500029g>.
- [10] Adeyemi S. Adeleye, Jon R. Conway, Kendra Garner, Yuxiong Huang, Yiming Su, Arturo A. Keller, Engineered nanomaterials for water treatment and remediation: costs, benefits, and applicability, *Chem. Eng. J.* 286 (2016) 640–662, <https://doi.org/10.1016/j.cej.2015.10.105>.
- [11] T. Paunesku, T. Rajh, G. Wiederrecht, J. Maser, S. Vogt, N. Stojićević, M. Protić, B. Lai, J. Oryhon, M. Thurnauer, G. Woloschak, Biology of TiO<sub>2</sub>-oligonucleotide nanocomposites, *Nat. Mater.* 2 (2003) 343–346, <https://doi.org/10.1038/nmat875>.
- [12] A. Malhotra Tallury, L.M. Byrne, S. Santra, Nanobioimaging and sensing of infectious diseases, *Adv. Drug Deliv. Rev.* 62 (2010) 424–437, <https://doi.org/10.1016/j.addr.2009.11.014>.
- [13] S. Sakib, R. Pandey, L. Soleymani, I. Zhitomirsky, Surface modification of TiO<sub>2</sub> for photoelectrochemical DNA biosensors, *Med. Devices Sens.* 3 (2020) e10066, <https://doi.org/10.1002/mds3.10066>.
- [14] S. Motta, P. Siani, E. Donadoni, G. Frigerio, L. Bonati, C. Di Valentin, Metadynamics simulations for the investigation of drug loading on functionalized inorganic nanoparticles, *Nanoscale* 15 (2023) 7909–7919, <https://doi.org/10.1039/D3NR00397C>.
- [15] G. Frigerio, E. Donadoni, P. Siani, J. Vertemara, S. Motta, L. Bonati, L. De Gioia, C. Di Valentin, Mechanism of RGD-conjugated nanodevice binding to its target protein integrin  $\alpha\beta3$  by atomistic molecular dynamics and machine learning, *Nanoscale* 16 (2024) 4063–4081, <https://doi.org/10.1039/D3NR05123D>.
- [16] P. Siani, C. Di Valentin, Effect of dopamine-functionalization, charge and pH on protein corona formation around TiO<sub>2</sub> nanoparticles, *Nanoscale* 14 (2022) 5121, <https://doi.org/10.1039/D1NR07647G>.
- [17] X. Zhang, F. Wang, B. Liu, E.Y. Kelly, M.R. Servos, J. Liu, Adsorption of DNA Oligonucleotides by Titanium Dioxide Nanoparticles, *Langmuir* 30 (2014) 839–845, <https://doi.org/10.1021/la404633p>.
- [18] H. Suzuki, T. Amano, T. Toyooka, Y. Ibuki, Preparation of DNA-Adsorbed TiO<sub>2</sub> Particles with High Performance for Purification of Chemical Pollutants, *Environ. Sci. Technol.* 42 (2008) 8076–8082, <https://doi.org/10.1021/es800948d>.
- [19] I. Sit, E. Quirk, E. Hettiarachchi, V.H. Grassian, Differential Surface Interactions and Surface Templating of Nucleotides (dGMP, dCMP, dAMP, and dTMP) on Oxide Particle Surfaces, *Langmuir* 38 (2022) 15038–15049, <https://doi.org/10.1021/acs.langmuir.2c01604>.
- [20] Levina A, M. Repkova, Z. Ismagilov, High-performance method for specific effect on nucleic acids in cells using TiO<sub>2</sub>-DNA nanocomposites, *Sci. Rep.* 2 (2012) 756, <https://doi.org/10.1038/srep00756>.
- [21] A.N. Enyashin Gemming, J. Frenzel, G. Seifert, Adsorption of nucleotides on the rutile (110) surface, *Int. J. Mater. Research* 101 (2010) 758–764, <https://doi.org/10.3139/146.110337>.
- [22] S. Monti, T.R. Walsh, Molecular Dynamics Simulations of the Adsorption and Dynamical Behavior of Single DNA Components on TiO<sub>2</sub>, *J. Phys. Chem. C* 115 (2011) 24238–24246, <https://doi.org/10.1021/jp207950p>.
- [23] F.A. Soria, C. Di Valentin, Binding group of oligonucleotides on TiO<sub>2</sub> surfaces: phosphate anions or nucleobases? *Appl. Surf. Sci.* 575 (2022) 151560, <https://doi.org/10.1016/j.apsusc.2021.151560>.
- [24] F. De Angelis, C. Di Valentin, S. Fantacci, A. Vittadini, A. Selloni, Theoretical Studies on Anatase and Less Common TiO<sub>2</sub> Phases: bulk, Surfaces, and Nanomaterials, *Chem. Rev.* 114 (2014) 9708–9753, <https://doi.org/10.1021/cr500055q>.
- [25] A.P. Thompson, H.M. Aktulga, R. Berger, D.S. Bolintineanu, W.M. Brown, P. S. Crozier, P.J. in 't Veld, A. Kohlmeyer, S.G. Moore, T.D. Nguyen, R. Shan, M. J. Stevens, J. Tranchida, C. Trott, S.J. Plimpton, LAMMPS - a flexible simulation tool for particle-based materials modeling at the atomic, meso, and continuum scales, *Comp Phys Comm* 271 (2022) 10817, <https://doi.org/10.1016/j.cpc.2021.108171>.
- [26] M. Matsui, M. Akaogi, Molecular Dynamics Simulations of the Structural and Physical Properties of the Four Polymorphs of TiO<sub>2</sub>, *Mol. Simul.* 6 (1991) 239–244, <https://doi.org/10.1080/08927029108022432>.
- [27] P. Siani, L. Ferraro S.Motta, A.O. Dohn, C. Di Valentin, Dopamine-Decorated TiO<sub>2</sub> Nanoparticles in Water: a QM/MM vs an MM Description, *J. Chem. Theory. Comput.* 16 (2020) 6560–6574, <https://doi.org/10.1021/acs.jctc.0c00483>.
- [28] T. Huynh Luan, R. Zhou, Simplified TiO<sub>2</sub> force fields for studies of its interaction with biomolecules, *J. Chem. Phys.* 142 (2015) 234102, <https://doi.org/10.1063/1.4922618>.
- [29] K. Hart, N. Foloppe, C.M. Baker, E.J. Denning, L. Nilsson, A.D. MacKerell Jr., Optimization of the CHARMM Additive Force Field for DNA: improved Treatment of the BI/BI Conformational Equilibrium, *J. Chem. Theory. Comput.* 8 (2012) 348–362, <https://doi.org/10.1021/ct200723y>.
- [30] A.D. MacKerell Jr., D. Bashford, M. Bellott, R.L. Dunbrack Jr., J.D. Evanseck, M. J. Field, S. Fischer, J. Gao, H. Guo, S. Ha, D. Joseph-McCarthy, L. Kuchnir, K. Kuczyka, F.T.K. Lau, C. Mattos, S. Michnick, T. Ngo, D.T. Nguyen, B. Prodhom, W.E. Reiher, B. Roux, M. Schlenkerich, J.C. Smith, R. Stote, J. Straub, M. Watanabe, J. Wórkiewicz-Kuczera, D. Yin, M. Karplus, All-Atom Empirical Potential for Molecular Modeling and Dynamics Studies of Proteins, *J. Phys. Chem. B* 102 (1998) 3586–3616, <https://doi.org/10.1021/jp973084f>.
- [31] A.I. Jewett, D. Stelter, J. Lambert, S.M. Saladi, O.M. Roscioni, M. Ricci, L. Autin, M. Maritan, S.M. Bashusqeh, T. Keyes, R.T. Dame, J.-E. Shea, G.J. Jensen, D. S. Goodsell, Moltemplate: a Tool for Coarse-Grained Modeling of Complex Biological Matter and Soft Condensed Matter Physics, *J. Mol. Biol.* 433 (2021) 166841, <https://doi.org/10.1016/j.jmb.2021.166841>.
- [32] M.D. Hanwell, D.E. Curtis, D.C. Lonie, E. Zurek, T. Vandermeersch, G.R. Hutchison, Avogadro: an advanced semantic chemical editor, visualization, and analysis platform, *J. Cheminform.* 4 (2012) 17, <https://doi.org/10.1186/1758-2946-4-17>.
- [33] S. Jo, X. Cheng, S.M. Islam, L. Huang, H. Rui, A. Zhu, H.S. Lee, Y. Qi, W. Han, K. Vanommeslaeghe, A.D. MacKerell Jr., B. Roux, W. Chapter eight - CHARMM-GUI PDB Manipulator for Advanced Modeling and Simulations of Proteins Containing Non-standard Residues, *Adv. Protein Chem. Struct. Biol.* 96 (2014) 235–265, <https://doi.org/10.1016/b.sapscb.2014.06.002>.
- [34] A.K. Manna, S.K. Pati, Theoretical understanding of single-stranded DNA assisted dispersion of graphene, *J. Mater. Chem. B* 1 (2013) 91–100.
- [35] B. Luan, R. Zhou, Spontaneous ssDNA stretching on graphene and hexagonal boron nitride in plane heterostructures, *Nat. Commun.* 10 (2019) 4610.
- [36] Y. Cheng, N. Korolev, L. Nordenskiöld, Similarities and differences in interaction of K<sup>+</sup> and Na<sup>+</sup> with condensed ordered DNA, *Mol. Dyn. Comput. Simul. Stud. Nucl. Acids Research* 34 (2006) 686–696, <https://doi.org/10.1093/nar/gkj434>.
- [37] K. Chakraborty, P. Khatua S. Bandyopadhyay, Exploring ion induced folding of a single-stranded DNA oligomer from molecular simulation studies, *Phys. Chem. Chem. Phys.* 18 (2016) 15899–15910, <https://doi.org/10.1039/C6CP00663A>.
- [38] P. Siani, G. Frigerio, E. Donadoni, C. Di Valentin Modeling Zeta, Potential for Nanoparticles in Solution: water Flexibility Matters, *J. Phys. Chem. C* 127 (2023) 9236–9247, <https://doi.org/10.1021/acs.jpcc.2c08988>.
- [39] M.K. Ridley, M.L. Machesky, D.A. Palmer, D.J. Wesolowski, Potentiometric Studies of The Rutile–Water Interface: hydrogen-Electrode Concentration-Cell Versus Glass-Electrode Titrations, *Colloids Surf. A* 204 (2002) 295–308, [https://doi.org/10.1016/S0927-7757\(02\)00017-1](https://doi.org/10.1016/S0927-7757(02)00017-1).
- [40] K.C. Akrapotulu, C. Kordulis, A. Lycourghiotis, Effect of Temperature on the Point of Zero Charge and Surface Charge of TiO<sub>2</sub>, *J. Chem. Soc., Faraday Trans* 86 (1990) 3437–3440, <https://doi.org/10.1039/f9908603437>.
- [41] A. Vakurov, R. Drummond-Brydson, O. Ugwuinsachi, A. Nelson, Significance of Particle Size and Charge Capacity in TiO<sub>2</sub> Nanoparticle-Lipid Interactions, *J. Colloid Interface Sci.* 473 (2016) 75–83, <https://doi.org/10.1016/j.jcis.2016.03.045>.
- [42] L. Martínez, R. Andrade, E.G. Birgin, J.M. Martínez, PACKMOL: a package for building initial configurations for molecular dynamics simulations, *J. Comput. Chem.* 30 (2009) 2157–2164, <https://doi.org/10.1002/jcc.21224>.
- [43] J.-P. Ryckaert, G. Cicciotti, H.J.C. Berendsen, Numerical integration of cartesian equations of motion of a system with constraints - molecular dynamics of N-alkanes, *J. Comput. Phys.* 23 (1977) 327–341, [https://doi.org/10.1016/0021-9991\(77\)90098-5](https://doi.org/10.1016/0021-9991(77)90098-5).
- [44] R.W. Hockney, J.W. Eastwood, Computer Simulation Using Particles, 1st ed., CRC Press, Boca Raton, 1988 <https://doi.org/10.1201/9780367806934>.
- [45] W. Humphrey, A. Dalke, K. Schulten, VMD: visual molecular dynamics, *J. Mol. Graphics* 14 (1996) 33–38, [https://doi.org/10.1016/0263-7855\(96\)00018-5](https://doi.org/10.1016/0263-7855(96)00018-5).
- [46] R.M. Elder, A. Jayaraman, Simulation study of the effects of surface chemistry and temperature on the conformations of ssDNA oligomers near hydrophilic and hydrophobic surfaces, *J. Chem. Phys.* 140 (2014) 155103, <https://doi.org/10.1063/1.4870776>.

- [47] S. Muraru, C. Gabriel, G. Samoila, E.I. Slusanschi, J.S. Burns, Molecular Dynamics Simulations of DNA Adsorption on Graphene Oxide and Reduced Graphene Oxide-PEG-NH<sub>2</sub> in the Presence of Mg<sup>2+</sup> and Cl<sup>-</sup> ions, *Coatings* 10 (2020) 289, <https://doi.org/10.3390/coatings10030289>.
- [48] Z. Xu, X. Lei, Y. Tu, Z.-J. Tan, B. Song, H. Fang, Dynamic Cooperation of Hydrogen Binding and  $\pi$  Stacking in ssDNA Adsorption on Graphene Oxide, *Chem. Eur. J.* 23 (2017) 13100, <https://doi.org/10.1002/chem.201701733>.
- [49] H. Ma, Z. Xu, H. Fang, X. Lei, Unexpected sequence adsorption features of polynucleotide ssDNA on graphene oxide, *Phys. Chem. Chem. Phys.* 22 (2020) 11740–11746, <https://doi.org/10.1039/D0CP01066A>.
- [50] I.C. Yeh, G. Hummer, Diffusion and Electrophoretic Mobility of Single-Stranded RNA from Molecular Dynamics Simulations, *Biophys. J.* 86 (2004) 681–689, [https://doi.org/10.1016/S0006-3495\(04\)74147-8](https://doi.org/10.1016/S0006-3495(04)74147-8).
- [51] D.Ž. Veljković, V.B. Medaković, J.M. Andrić, S.D. Zarić, C-H/O interactions of nucleic bases with a water molecule: a crystallographic and quantum chemical study, *CrystEngComm.* 16 (2014) 10089, <https://doi.org/10.1039/C4CE00595C>.
- [52] D.Ž. Veljković, Strong C-H/O interactions between polycyclic aromatic hydrocarbons and water: influence of aromatic system size, *J. Mole. Graph. Model.* 80 (2018) 121–125.
- [53] O. Takahashi, Y. Kohno, M. Nishio, Relevance of Weak Hydrogen Bonds in the Conformation of Organic Compounds and Bioconjugates: evidence from Recent Experimental Data and High-Level ab Initio MO Calculations, *Chem. Rev.* 110 (2010) 6049–6076, <https://doi.org/10.1021/cr100072x>.
- [54] D. Hayakawa, N. Sawada, Y. Watanabe, H. Gouda, A molecular interaction field describing nonconventional intermolecular interactions and its application to protein–ligand interaction prediction, *J. Mole. Graph. Model.* 96 (2020) 107515, <https://doi.org/10.1016/j.jmglm.2019.107515>.
- [55] S. Zeng, L. Chen, Y. Wang, J. Chen, Exploration on the mechanism of DNA adsorption on graphene and graphene oxide via molecular simulations, *J. Phys. D: Appl. Phys.* 48 (2015) 275402, <https://doi.org/10.1088/0022-3727/48/27/275402>.
- [56] E. Jurrus, D. Engel, K. Star, K. Monson, J. Brandi, L.E. Felberg, D.H. Brookes, L. Wilson, J. Chen, K. Liles, M. Chun, P. Li, D.W. Gohara, T. Dolinsky, R. Konecny, D.R. Koes, J.E. Nielsen, T. Head-Gordon, W. Geng, R. Krasny, G.W. Wei, M.J. Holst, J.A. McCammon, N.A. Baker, Improvements to the APBS biomolecular solvation software suite, *Protein Sci.* 27 (2018) 112–128, <https://doi.org/10.1002/pro.3280>.